Solvent-Free Synthesis of Uniform MOF Shell-Derived Carbon Confined SnO_2/Co Nanocubes for Highly Reversible Lithium Storage

Qiu He, Jinshuai Liu, Zhaohuai Li, Qi Li, Lin Xu, Baoxuan Zhang, Jiashen Meng, Yuzhu Wu, and Liqiang Mai**

Tin dioxide (SnO_2) has attracted much attention in lithium-ion batteries (LIBs) due to its abundant source, low cost, and high theoretical capacity. However, the large volume variation, irreversible conversion reaction limit its further practical application in next-generation LIBs. Here, a novel solvent-free approach to construct uniform metal–organic framework (MOF) shell-derived carbon confined SnO_2/Co (SnO_2/Co@C) nanocubes via a two-step heat treatment is developed. In particular, MOF-coated $CoSnO_3$ hollow nanocubes are for the first time synthesized as the intermediate product by an extremely simple thermal solid-phase reaction, which is further developed as a general strategy to successfully obtain other uniform MOF-coated metal oxides. The as-synthesized SnO_2/Co@C nanocubes, when tested as LIB anodes, exhibit a highly reversible discharge capacity of 800 mAh g^{-1} after 100 cycles at 200 mA g^{-1} and excellent cycling stability with a retained capacity of 400 mAh g^{-1} after 1800 cycles at 5 A g^{-1}. The experimental analyses demonstrate that these excellent performances are mainly ascribed to the delicate structure and a synergistic effect between Co and SnO_2. This facile synthetic approach will greatly contribute to the development of functional metal oxide-based and MOF-assisted nanostructures in many frontier applications.

1. Introduction

With the advantages of high energy density, long lifespan, nil memory effect, and environmental benignity, lithium-ion batteries (LIBs) have become the most promising power sources for mobile electronic devices and stationary energy storage systems for green energy.[1–8] With the fast consumption of energy, more efficient LIBs with higher rate and capacity are greatly desired. SnO_2 anode is viewed as a potential substitute of graphite to achieve both high specific capacity and superior rate capacity of LIBs, owing to its high theoretical capacity (782 mAh g^{-1}), low potential for Li^+ insertion, low toxicity, and low cost.[9,10] However, its practical application is hindered by two fatal issues. One is the intrinsically low initial Coulombic efficiency due to the irreversible conversion of SnO_2 to Sn in the first discharge process. The other is the large volume expansion (≈300% upon full lithiation) caused by the formation of the alloy Li_xSn ($0 < x \leq 4.4$), which eventually results in the pulverization of electrodes and the related fast capacity fading during cycling.[11]

Many efforts have been devoted to solving the aforementioned issues. One feasible approach is constructing porous, nanosized, and hollow structures of SnO_2. Li et al.[12]

Q. He, J. S. Liu, Z. H. Li, Dr. Q. Li, Dr. L. Xu, B. X. Zhang, J. S. Meng, Y. Z. Wu, Prof. L. Q. Mai
State Key Laboratory of Advanced Technology for Materials Synthesis and Processing
Wuhan University of Technology
Wuhan, 430070 Hubei, P. R. China
E-mail: qi.li@whut.edu.cn; mlq518@whut.edu.cn
Prof. L. Q. Mai
Department of Chemistry
University of California
Berkeley, CA 94720, USA

The ORCID identification number(s) for the author(s) of this article can be found under https://doi.org/10.1002/smll.201701504.

DOI: 10.1002/smll.201701504

reported mesoporous hollow SnO_2 nanococoons with an average size of 20 nm; Lou et al.[13,14] designed nanoboxes and hollow nanospheres; Park et al.[15] synthesized randomly aligned SnO_2 nanowires with diameters of 200–500 nm. The ultrasmall sizes of SnO_2 or introduced interspaces in these structures are greatly beneficial for reducing the ion diffusion paths and thus enhancing the reaction kinetics, as well as relieving the volume expansion and the accompanying internal stress. Another effective method is compositing SnO_2 with carbon, such as coaxial carbon-coated SnO_2 hollow nanospheres,[16] hierarchically porous carbon encapsulated SnO_2 nanocrystals,[17] and N-doped carbon-coated SnO_2 sub-microboxes and SnO_2 nanofibers.[18,19] It was confirmed that the carbon shell can prominently enhance the conductivity, stabilize the solid-electrolyte interphase (SEI), and maintain the mechanical integrity. Moreover, to increase the coulombic efficiency and to stabilize the nanostructure of the SnO_2 anodes, hybridizing SnO_2 with nanosized transition metals for a synergistic effect has been used as an efficient strategy.[20,21] Hu et al.[22] demonstrated that the incorporated metals (M = Fe, Mn, Co) could accelerate the decomposition of Li_2O because the conversion of M/Li_2O to MO suffers a much lower energy barrier than that of Sn/Li_2O to SnO_2, and concurrently impede the agglomeration of Sn. As a result, the inert Li_2O wrapped Sn was released so as to promote the conversion of Sn to SnO_2, and the structural stability was improved. However, it is still a tough challenge to synthesize SnO_2-based anode materials with both high specific capacity and stable cycling performance. In this regard, a strategy to combine the aforementioned problem-solving approaches to meet this challenge and facilitate the scalable application of SnO_2-based anodes is of great significance.

Metal–organic frameworks (MOFs) constructed by metal ions/clusters and organic linkers via coordination bonding show great potential in energy storage because of their homogeneous morphologies, small sizes, porous structures, and large specific surface areas.[23–25] When used in energy storage, MOF-derived nanoporous carbon shell can not only enhance the mechanical integrity and the conductivity of the structure but also allow for fast transference of Li^+ and store Li^+ ions via an adsorption mechanism.[26] As Zhang et al.[27] reported about the ZnO@ZnO quantum dots/C core–shell nanorod arrays on a carbon cloth, the MOF-derived carbon shell greatly contributed to their excellent electrochemical performance in LIBs. However, the adopted solution method is difficult to obtain a uniform MOF shell, and inevitably involves a tedious synthesis process.[28,29]

Herein, to avoid the aforementioned deficiencies, we developed a simple two-step, solvent-free heat treatment to synthesize MOF shell-derived carbon confined SnO_2/Co (SnO_2/Co@C) nanocubes. The adopted solid-phase synthesis method is more environment friendly without using a large amount of organic solvent, thus cutting down the cost of production and avoiding the serious pollution. Besides, the operation of solid-phase synthesis is simpler and more time-saving without washing and drying process. In detail, uniform MOF-coated $CoSnO_3$ ($CoSnO_3$@MOF) hollow nanocubes were first synthesized by a thermal solid-phase reaction, and then after carbonization, the obtained $CoSnO_3$@MOF nanocubes were converted into SnO_2/Co@C nanocubes. When tested as an anode material for LIBs, the as-synthesized SnO_2/Co@C nanocubes possess a high reversible capacity of 800 mAh g^{-1} after 100 cycles at 200 mA g^{-1} and a long-term stable capacity of 400 mAh g^{-1} after 1800 cycles at 5 A g^{-1}. The excellent performance can be attributed to the unique characteristics of SnO_2/Co@C nanocubes including small sizes, abundant interspaces, contained Co, and uniform porous carbon shell. In addition, to our best knowledge, it is the first time to report a uniform MOF-coated metal oxide acquired by a simple thermal solid-phase reaction. To demonstrate the generality of our concept of synthesis, this simple method is further extended to ZnO and $Zn_3V_2O_8$.

2. Results and Discussion

The SnO_2/Co@C nanocubes were synthesized by a solvent-free synthesis process, as the schematic illustration shown in **Figure 1**. First, the mixture of hollow $CoSn(OH)_6$ and abundant 1,4-benzenedicarboxylic acid (H_2BDC) undertook step I heat treatment in air which involves two successive stages: 1 h at 300 °C for a rational coordination reaction; 0.5 h at 320 °C to remove unreacted H_2BDC. Hollow $CoSn(OH)_6$ nanocubes acted as the precursor, which can be easily synthesized by a simple coprecipitation method.[30,31] The obtained $CoSn(OH)_6$ nanocubes show high crystallinity and homogeneous morphology with the edge length of ≈150 nm (Figure S1a–c, Supporting Information). H_2BDC was chosen as the organic linker and it can volatilize at 320 °C without melting so that the agglomeration and additional reaction of solid–liquid phase could be avoided. During the Step-I heat treatment, two reactions happened. One is the pyrolysis of $CoSn(OH)_6$ at around 200 °C, which is confirmed by the thermogravimetric analysis (TGA) of $CoSn(OH)_6$ (Figure S2, Supporting Information). The pyrolysis reaction can be described by the following equation[32–34]

$$CoSn(OH)_6 \rightarrow CoSnO_3 + 3H_2O \quad (1)$$

The weight loss of $CoSn(OH)_6$ at 110–275 °C is measured to be 19.4%, which is very close to the theoretical mass fraction (19.3%) of the produced water based on Equation (1). The other reaction is the coordination reaction between Co ions and organic ligands in H_2BDC, which leads to the formation of a MOF layer on $CoSnO_3$ nanocubes. Owing to the intrinsic slow ion transportation in solid and thus low reaction rate of solid-phase reaction, the coordination just took place on the surfaces/interfaces of the nanocubes. Accordingly, a thin film of amorphous MOF was produced on the surface of the nanocubes. Finally, the generated $CoSnO_3$@MOF hollow nanocubes were calcinated at 550 °C in argon in the Step II heat treatment to obtain the SnO_2/Co@C nanocubes. In this step, the organic ligands in the MOF film were *in situ* carbonized and the porous carbon shell was formed.

As shown in the scanning electron microscopy (SEM) and the transmission electron microscopy (TEM) images (**Figure 2**a,b), the $CoSnO_3$@MOF hollow nanocubes well

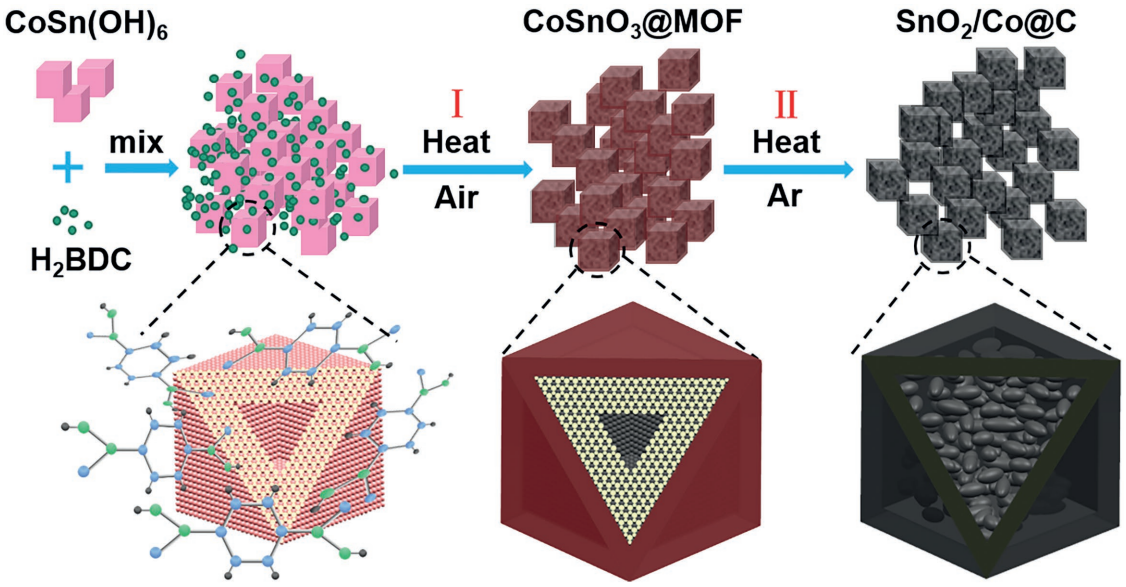

Figure 1. Schematic illustration of the solvent-free synthesis process of SnO_2/Co@C nanocubes.

maintain the cubic shape of the $CoSn(OH)_6$ precursor after the step I heat treatment. The hollow interior and a thin shell are clearly observed. The corresponding energy-dispersive X-ray (EDX) mapping images (Figure 2c) confirm the coexistence of C, O, Sn, and Co in the $CoSnO_3$@MOF nanocubes. The inner part is $CoSnO_3$ and the outer thin layer is believed to be MOF. The X-ray diffraction (XRD) pattern (Figure S3, Supporting Information) indicates that the $CoSnO_3$@MOF is amorphous. In order to confirm the occurrence of the coordination reaction, the Fourier transform infrared (FT-IR) analysis was carried out and the FT-IR transmittance spectra of $CoSn(OH)_6$, H_2BDC, and $CoSnO_3$@MOF are shown in Figure 2d. The vibrational peaks of benzene rings and ester groups are observed in the $CoSnO_3$@MOF nanocubes,[35,36] suggesting some organic groups originating from H_2BDC are kept due to the coordination reaction.

To further confirm the existence of the MOF, X-ray photoelectron spectroscopy (XPS) analysis was performed to characterize the composition within ≈10 nm beneath the surfaces of $CoSnO_3$@MOF hollow nanocubes. The XPS spectra of $CoSn(OH)_6$ and $CoSnO_3$@MOF are shown in Figure 2e. $CoSnO_3$@MOF hollow nanocubes exhibit a newly emerged strong peak of C 1s and a relatively stronger peak of O 1s (compared with Sn 3d) than $CoSn(OH)_6$, corresponding to that abundant organic groups derived from H_2BDC distribute on the surface of $CoSnO_3$@MOF nanocubes.[37,38] The detailed relative atomic contents of C, Sn, O, and Co of $CoSn(OH)_6$ and $CoSnO_3$@MOF are displayed in Figure 2f. The unexpectedly detected trace amount of C in $CoSn(OH)_6$ is ascribed to the intrinsically introduced carbon source in XPS tests. The ratio of Sn, O, and Co atomic contents of $CoSn(OH)_6$ is close to the theoretical one of 1:6:1. In contrast, the almost disappeared Sn, the abundant carbon, and the rationally diminished Co and O are detected in $CoSnO_3$@MOF, suggesting the existence of the MOF which contains C, Co, O and encapsulates $CoSnO_3$ inside. The result agrees with the sharply gained relative peak intensity of Co in $CoSnO_3$@MOF in Figure 2e, which demonstrates the transport of Co ions from interior to exterior and that Sn ions are kept inside without participating in the coordination reaction. The comparison of high-resolution C 1s spectra between $CoSnO_3$@MOF and H_2BDC is displayed in Figure 2g. The C 1s spectrum of H_2BDC is resolved into two compounds: the C=C from benzene rings at 284.4 eV and C=O from ester groups at 288.8 eV.[39,40] In the C 1s spectrum of $CoSnO_3$@MOF hollow nanocubes, the peaks of C=C and C=O are preserved. In addition, a distinct newly generated C−O peak at 285.6 eV is observed, further indicating the occurrence of the coordination reaction where the carboxyls of H_2BDC break up and link to Co ions with generating C−O bands.

After the Step II calcination, the SnO_2/Co@C nanocubes perfectly retain the morphology of nanocubes. The SEM image of monodispersed SnO_2/Co@C nanocubes with the edge length of ≈180 nm is shown in **Figure 3**a. There is a slight increase in size compared to $CoSn(OH)_6$ nanocubes owing to the porous carbon shell. The TEM images of SnO_2/Co@C nanocubes (Figure 3b,c) show that SnO_2/Co nanoparticles are wrapped in the intact carbon shells. The rich internal cavities are clearly shown by contrast between SnO_2/Co nanoparticles and hollow interior. The corresponding elemental mappings (Figure 3d) obviously show the distribution of Sn, Co, O in the internal SnO_2/Co nanoparticles and C in the external carbon shell. The XPS spectrum of SnO_2/Co@C nanocubes (Figure S4a, Supporting Information) shows a very strong peak of C 1s due to the fully encapsulation of carbon layer. The high-resolution C 1s XPS spectrum (Figure S4b, Supporting Information) reveals that the carbon exists in three situations: C=O bond, C−O bond, and graphitic carbon.

The XRD pattern of SnO_2/Co@C nanocubes (Figure 3e) clearly manifests the existence of crystalline SnO_2 and Co. The high-resolution TEM (HRTEM) image (Figure 3f) shows the SnO_2/Co@C nanocube encapsulated in porous and amorphous carbon layer with a uniform thickness of ≈11 nm. The

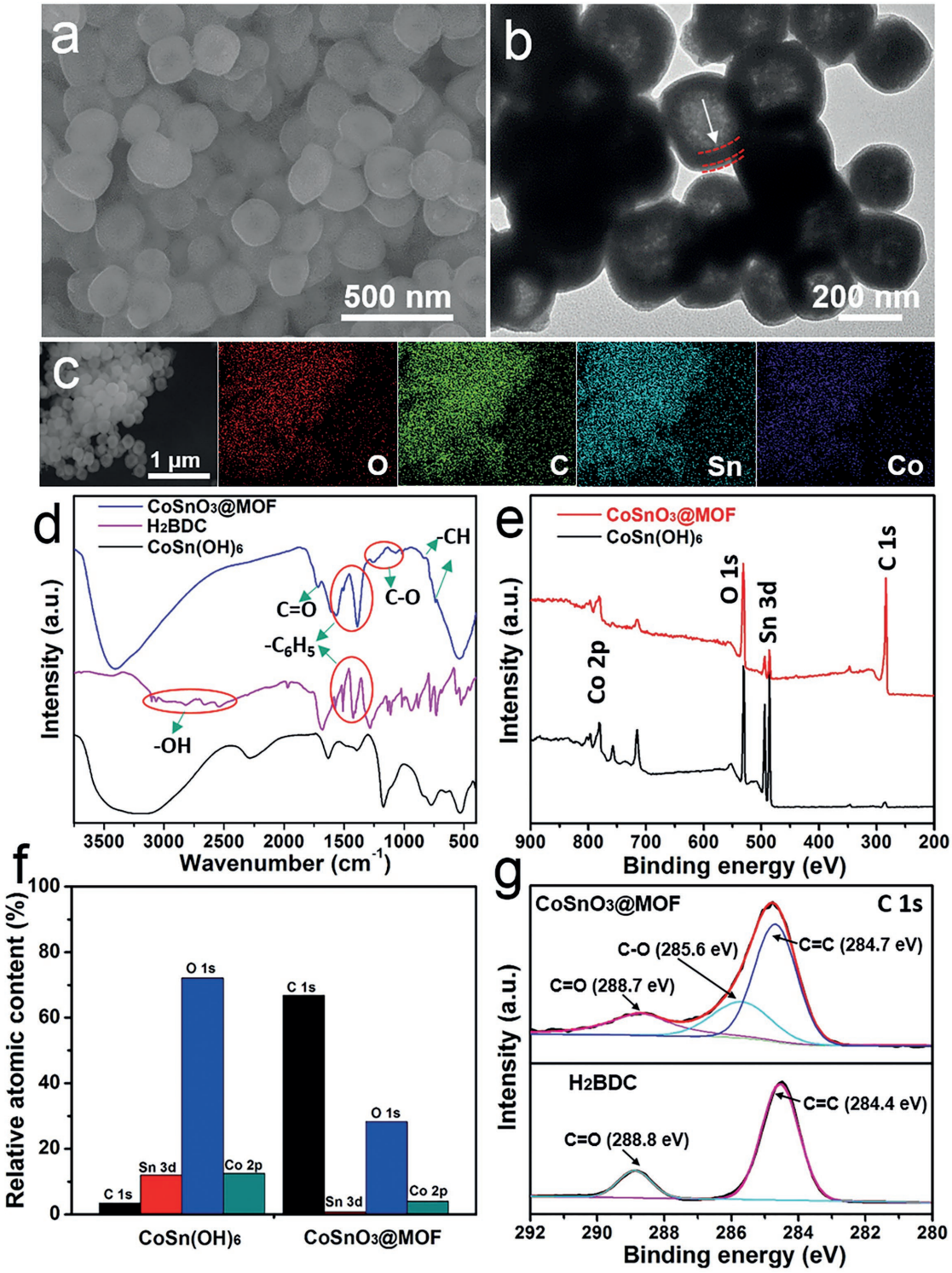

Figure 2. a) SEM image, b) TEM image, and c) EDX mapping images of $CoSnO_3$@MOF hollow nanocubes. d) FT-IR spectra of $CoSn(OH)_6$, H_2BDC, and $CoSnO_3$@MOF. e,f) XPS spectra and the corresponding relative atomic contents of C, Sn, O, and Co within ≈10 nm beneath the surfaces of $CoSn(OH)_6$ and $CoSnO_3$@MOF nanocubes, respectively. g) Comparison of C 1s spectra of $CoSnO_3$@MOF and H_2BDC.

measured interlayer distances of ≈0.33 and ≈0.20 nm are in agreement with the (110) plane of rutile SnO_2 and (111) plane of cubic Co, respectively. According to TGA of SnO_2/Co@C nanocubes (Figure S5a, Supporting Information), the weight fraction of the carbon shell is as low as 8.66%, suggesting a low content of the inactive component. Two broad peaks in the Raman spectrum of SnO_2/Co@C (Figure S5b, Supporting Information) located at around 1349 and 1585 cm^{-1} are assigned to the D (corresponds to disordered carbon or defective graphitic structures) and G (refers to graphitic carbon) bands of the carbon shell, respectively, further substantiating the partly graphitic nature of the carbon shell.[41]

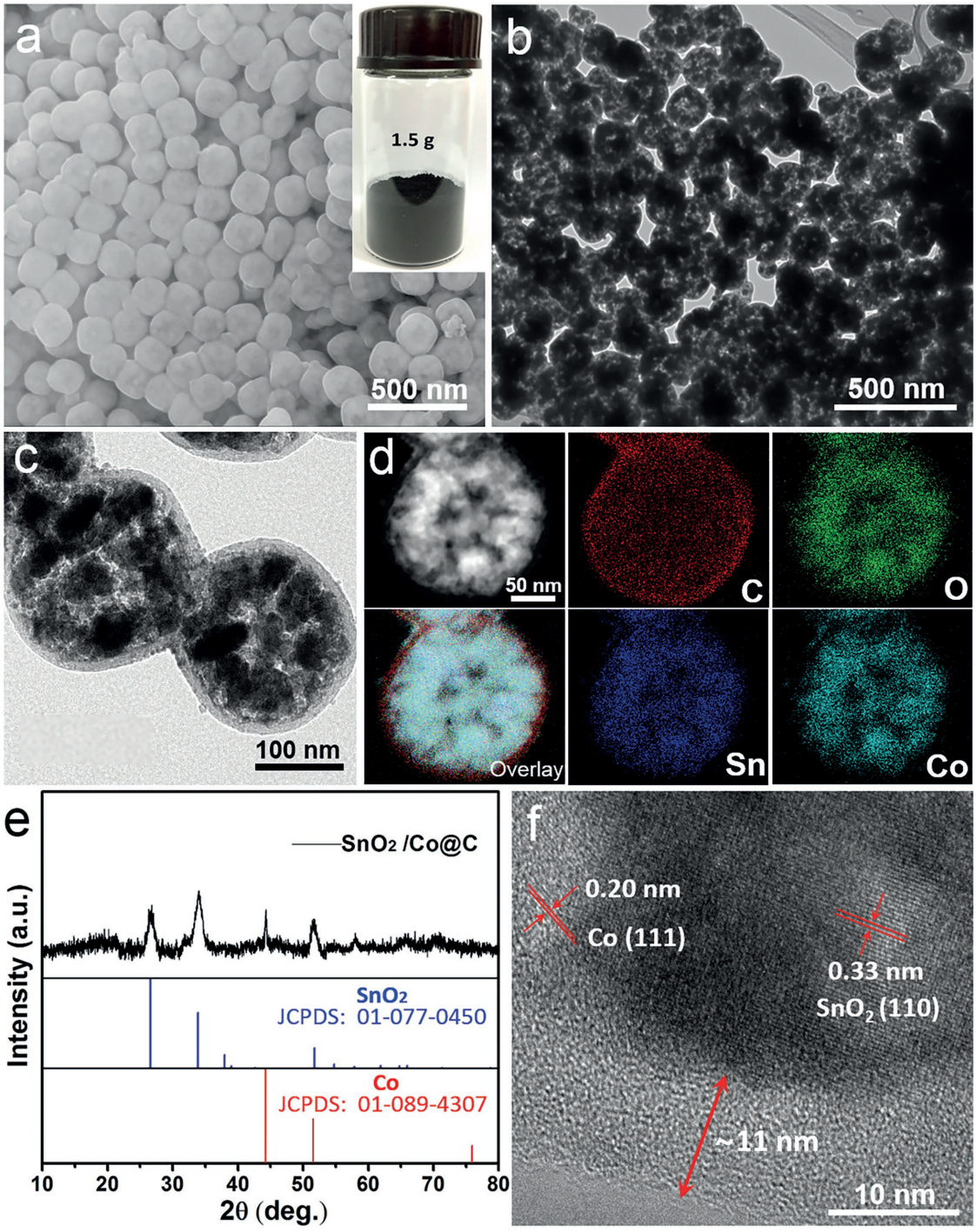

Figure 3. The characterizations of SnO_2/Co@C nanocubes: a) SEM image, the inset is the optical image; b,c) TEM images together with d) the corresponding elemental mappings; e) XRD pattern compared with those of standard SnO_2 and Co; and f) HRTEM image.

The N_2 adsorption/desorption isotherm and the corresponding pore size distribution of SnO_2/Co@C nanocubes based on the Barrett–Joyner–Halenda (BJH) model are shown in Figure S5c,d (Supporting Information). The SnO_2/Co@C nanocubes exhibit a relatively large Brunauer–Emmett–Teller (BET) surface area of 84 $m^2\ g^{-1}$ and the BJH pore volume of 0.15 $m^3\ g^{-1}$. The pore sizes mainly distribute in the mesopore range of 10–40 nm, while the larger pores could be ascribed to the continuous pore channels inside the nanocubes. The abundant void spaces provide rich reactive sites and effectively accommodate the volume expansion during Li^+ insertion.

It is worth mentioning that it is the first time to report a MOF-coated metal oxide acquired by a simple and scalable thermal solid-phase reaction, to our best knowledge. In this work, we further extend this method to synthesize ZnO@MOF and $Zn_3V_2O_8$@MOF. First, the precursors of ZnO microflowers and $Zn_3V_2O_7(OH)_2{\cdot}2H_2O$

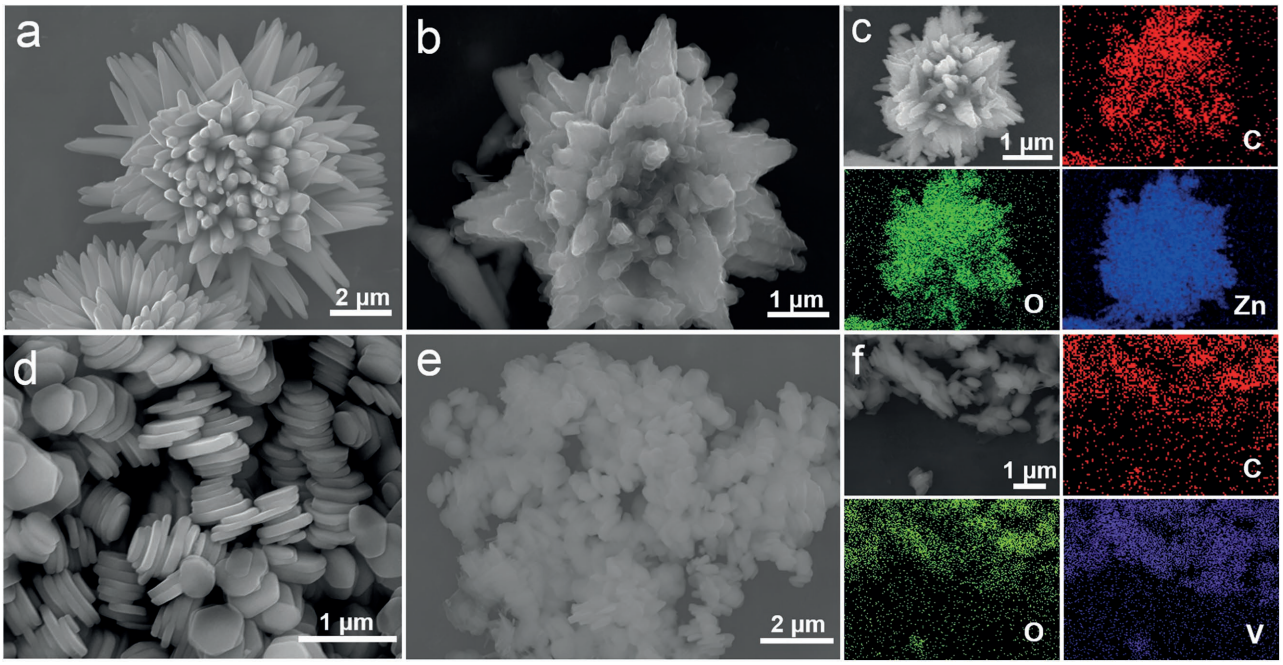

Figure 4. a) SEM image of ZnO microflowers; b,c) SEM image and the corresponding EDX mapping images of ZnO@MOF. d) SEM image of $Zn_3V_2O_7(OH)_2{\cdot}2H_2O$ nanoplates; e,f) SEM image and the corresponding EDX mapping images of $Zn_3V_2O_8$@MOF.

nanoplates with smooth surfaces and angular edges are synthesized (**Figure 4**a,d). Second, the ZnO microflowers and $Zn_3V_2O_7(OH)_2{\cdot}2H_2O$ nanoplates are mixed with abundant H_2BDC followed by the same heat treatment as $CoSn(OH)_6$ to obtain ZnO@MOF and $Zn_3V_2O_8$@MOF, respectively. As the XRD patterns presented in Figure S6a,b (Supporting Information), both ZnO and $Zn_3V_2O_7(OH)_2{\cdot}2H_2O$ exhibit high crystallinity. Apart from reacting with H_2BDC via the coordination between Zn ions and organic ligands on the surfaces, $Zn_3V_2O_7(OH)_2{\cdot}2H_2O$ was partially pyrolyzed generating $Zn_3V_2O_8$,[42] which is slightly different to ZnO which has a better thermostability. There are several weak peaks at small angles in the XRD pattern of $Zn_3V_2O_8$@MOF, which may be due to a slight crystallization of MOF. The SEM images of ZnO@MOF and $Zn_3V_2O_8$@MOF are displayed in Figure 4b,e. Their edges become blurry and surfaces turn to be hazy after the reaction, and the corresponding EDX mapping images (Figure 4c,f) indicate that the carbon elements homogeneously distribute in ZnO@MOF and $Zn_3V_2O_8$@MOF, respectively. The existing carbon element originated from H_2BDC confirms the coordination between metal ions and organic groups. This new and simple strategy to introduce a MOF coating layer may be applied to other materials for different applications.

The electrochemical performance of SnO_2/Co@C nanocubes as an anode material for LIBs has been evaluated. The cyclic voltammetry (CV) curves (**Figure 5**a) of the first three cycles were measured at a scan rate of 0.2 mV s^{-1} within the voltage window of 0.01–2.5 V. In the cathodic process, the representative unrepeatable peak at ≈0.76 V is caused by the initial conversion of SnO_2 to Sn, as described by Equation (2); the clearly discerned reductive peaks below 0.03 V can be assigned to the generation of Li_xSn alloy according to Equation (3); a slight sharp peak at ≈0.07 V that disappears in the following circles may be owing to the occurrence of side reactions between the anode and the electrolyte.[43,44] In contrast, the anodic peaks of Li_xSn dealloying process at 0.58 V and the oxidation of Co (Equation (4)) to generate CoO at 2.06 V show excellent reversibility.[45] A wide and Laigh peak at ≈1.28 V unveils a partial reversibility of Sn transforming to SnO_2[46–48]

$$SnO_2 + 4Li^+ + 4e^- \rightarrow 2Li_2O + Sn \quad (2)$$

$$Sn + xLi^+ + xe^- \leftrightarrow Li_xSn\ (0 < x \leq 4.4) \quad (3)$$

$$Co + Li_2O \rightarrow CoO + 2Li^+ + 2e^- \quad (4)$$

The cycling performance of SnO_2/Co@C nanocubes was performed using the charge/discharge galvanostatic cycling test from 0.01 to 2.5 V. As shown in Figure 5b, the first discharge capacity is ≈1300 mAh g^{-1} and the first charge capacity is ≈857 mAh g^{-1} at a current density of 200 mA g^{-1}, corresponding to the pretty high initial Coulombic efficiency of 66%. After cycling for 100 times, the reversible discharge capacity is 800 mAh g^{-1}, which equals to 93.3% of the first charge capacity. The 1st, 2nd, 10th, 50th, and 100th cycle charge–discharge voltage profiles of SnO_2/Co@C nanocubes at the current density of 200 mA g^{-1} are shown in Figure 5c. Distinct capacity decrease is only perceived in the first discharge process, and the following discharge profiles from 2th to 100th cycle remain almost unchanged, showing a good reversibility. The rate capability of SnO_2/Co@C nanocubes was measured by alternately discharging and charging at various current densities (Figure 5d). The corresponding charge–discharge voltage profiles are shown in Figure S7 (Supporting Information). Strikingly high reversible specific capacities of

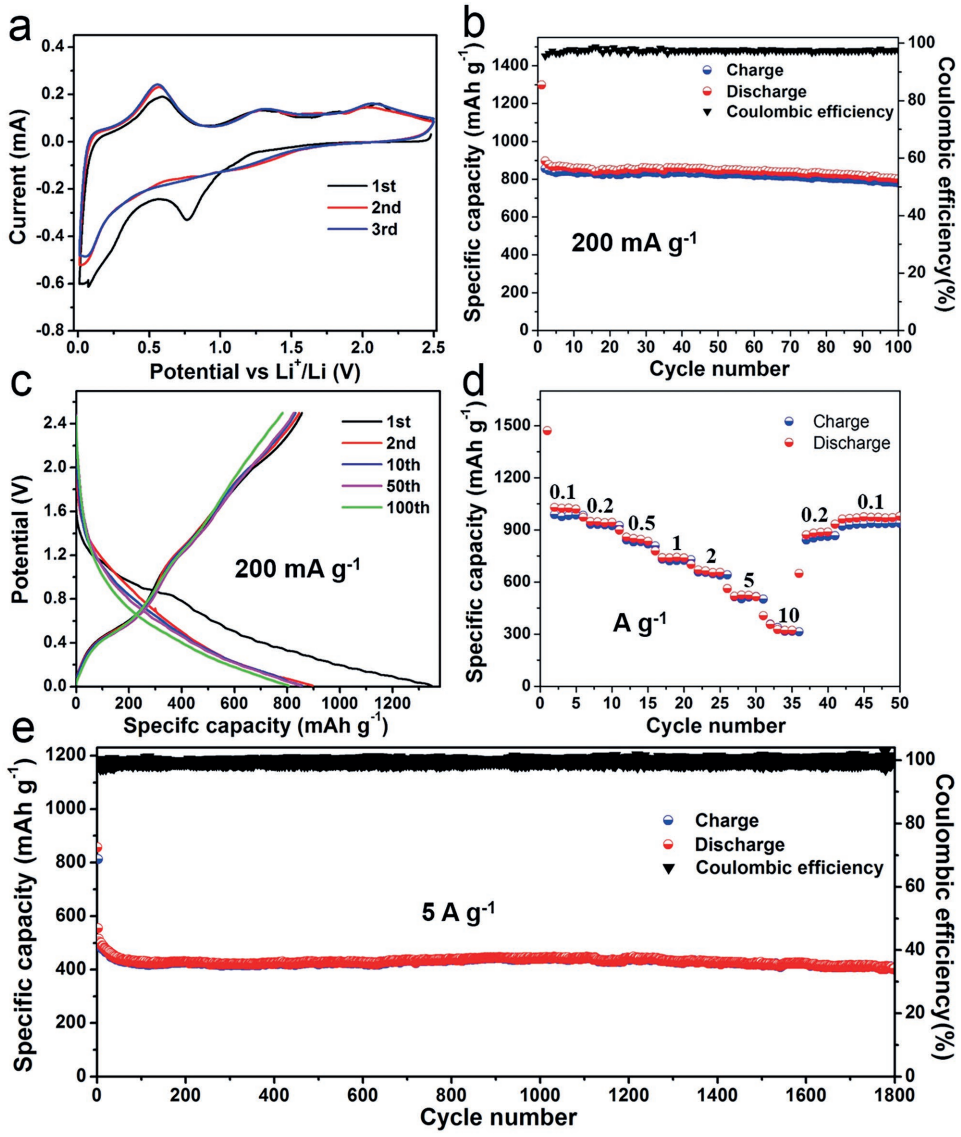

Figure 5. Electrochemical performance of SnO_2/Co@C nanocubes as an anode material for LIBs: a) CV curves of the first three cycles at the scan rate of 0.2 mV s^{-1}; b) cycling performance and corresponding Coulombic efficiency at the current density of 200 mA g^{-1}; c) charge–discharge voltage profiles for the 1st, 2nd, 10th, 50th, and 100th cycle at the current density of 200 mA g^{-1}; d) rate performance successively conducted at the current densities of 0.1, 0.2, 0.5, 1, 2, 5, and 10 A g^{-1}; e) long-term cycling performance and corresponding Coulombic efficiency at a galvanostatic measurements of a current density of 5 A g^{-1}. All tests were measured at the voltage range of 0.01–2.5 V, and all specific capacities are calculated based on the mass of SnO_2/Co@C.

≈1030, 950, 850, 740, 650, 520, and 350 mAh g^{-1} are delivered at the current densities of 0.1, 0.2, 0.5, 1, 2, 5, and 10 A g^{-1}, respectively. Moreover, the capacity quickly recovers to as high as 980 mAh g^{-1} when the current density is finally reduced back to 100 mA g^{-1}, suggesting extraordinary stability of the anode. The long-term cycling performance of the SnO_2/Co@C nanocubes and the corresponding Coulombic efficiency at a high current density of 5 A g^{-1} are displayed in Figure 5e. The noticeable decay only appears in the first 50 cycles, which may be ascribed to the SEI film stabilization and irreversible trapping of some lithium in the lattice. As seen from the cycling performance, the anode shows fabulous cycling stability and a high retained capacity of ≈400 mAh g^{-1} after 1800 cycles.

SnO_2/Co@C nanocubes as an anode material for LIBs exhibit superior electrochemical performance compared with some recently related reports (Table S1, Supporting Information), which results from their unique structure. On one hand, the nanosized structure and rich pores of SnO_2/Co@C nanocubes shorten the ion diffusion paths, accelerate the reaction kinetics, and effectively accommodate volume changes during cycling. The electrochemical impedance spectroscopy (EIS) plot (Figure S8, Supporting Information) indicates the charge-transfer resistance of the electrode based on SnO_2/Co@C nanocubes is ≈140 Ω, implying fast transportation of electrons and ions. On the other hand, the porous carbon shell with a close contact to the interior active materials not only enhances the conductivity but also confines SnO_2/Co nanoparticles within carbon shells and thus stabilizes the structure of the anode. The SEM image (Figure S9, Supporting Information) of SnO_2/Co@C nanocubes after cycling for 100 times at

200 mA g^{-1} shows the monodispersed nanocubes with a clearly identified carbon layer and rounded edges. The well-retained mechanical integrity is consistent with the superb cycling stability. What's more, except for promoting the conduction of electrons, the Co interspersed in SnO_2 prevents the migration and subsequent agglomeration of Sn during electrochemical cycling process, which enhances the structural stability and sustains the activity of Sn. The Co also consumes superfluous Li_2O with providing extra capacity, and releases the unavailable Sn wrapped by inert Li_2O to promote the reversible conversion of Sn. All these strategies together contribute to the high specific capacity, the extraordinary cycling performance, and the excellent rate capacity of the SnO_2/Co@C nanocubes.

3. Conclusions

In summary, a facile and scalable solvent-free approach has been developed for the first time to construct uniform carbon-confined SnO_2/Co nanocubes via a two-step heat treatment. The formation mechanism is clearly revealed and it mainly includes the formation of uniform MOF shell on metal oxides and *in situ* carbonization, which can be widely extended to other nanostructured metal oxides. As demonstrated, the as-prepared SnO_2/Co@C nanocubes possess excellent lithium storage property as an anode material in LIBs. Specifically, even tested at 5 A g^{-1} after 1800 cycles, these SnO_2/Co@C nanocubes displayed a long-term reversible capacity of 400 mAh g^{-1} with the capacity retention of ≈77%. This synthetic approach and proposed mechanism will open new avenues for the development of functional inorganics-carbon coupled materials for high-performance energy storage.

Supporting Information

Supporting Information is available from the Wiley Online Library or from the author.

Acknowledgements

Q.H. and J.S.L. contributed equally to this work. This work was supported by the National Key Research and Development Program of China (2016YFA0202603), the National Basic Research Program of China (2013CB934103), the Programme of Introducing Talents of Discipline to Universities (B17034), the National Natural Science Foundation of China (51521001), the National Natural Science Fund for Distinguished Young Scholars (51425204), and the Fundamental Research Funds for the Central Universities (WUT: 2016III001, 2017IVA100). L.Q.M. gratefully acknowledges financial support from China Scholarship Council (No. 201606955096).

Conflict of Interest

The authors declare no conflict of interest.

[1] F. Wang, X. Wu, C. Li, Y. Zhu, L. Fu, Y. Wu, X. Liu, *Energy Environ. Sci.* **2016**, *9*, 3611.
[2] L. Ji, Z. Lin, M. Alcoutlabi, X. Zhang, *Energy Environ. Sci.* **2011**, *4*, 2682.
[3] Z. Wang, L. Zhou, X. W. Lou, *Adv. Mater.* **2012**, *24*, 1903.
[4] J. I. Lee, H. Kang, K. H. Park, M. Shin, D. Hong, H. J. Cho, N. R. Kang, J. Lee, S. M. Lee, J. Y. Kim, *Small* **2016**, *12*, 3119.
[5] D. L. Ma, Z. Y. Cao, H. G. Wang, X. L. Huang, L. M. Wang, X. B. Zhang, *Energy Environ. Sci.* **2012**, *5*, 8538.
[6] X. L. Huang, R. Z. Wang, D. Xu, Z. L. Wang, H. G. Wang, J. J. Xu, Z. Wu, Q. C. Liu, Y. Zhang, X. B. Zhang, *Adv. Funct. Mater.* **2013**, *23*, 4345.
[7] C. Wu, J. Maier, Y. Yu, *Adv. Mater.* **2016**, *28*, 174.
[8] L. Xia, S. Wang, G. Liu, L. Ding, D. Li, H. Wang, S. Qiao, *Small* **2016**, *12*, 853.
[9] C. Wang, Y. Zhou, M. Ge, X. Xu, Z. Zhang, J. Z. Jiang, *J. Am. Chem. Soc.* **2010**, *132*, 46.
[10] Y. Zhang, L. Jiang, C. Wang, *Phys. Chem. Chem. Phys.* **2015**, *17*, 20061.
[11] S. M. Paek, E. Yoo, I. Honma, *Nano Lett.* **2009**, *9*, 72.
[12] L. Li, B. Guan, L. Zhang, Z. Su, H. Xie, C. Wang, *J. Mater. Chem. A* **2015**, *3*, 22021.
[13] Z. Wang, D. Luan, F. Y. Boey, X. W. Lou, *J. Am. Chem. Soc.* **2011**, *133*, 4738.
[14] X. W. Lou, Y. Wang, C. Yuan, J. Y. Lee, L. A. Archer, *Adv. Mater.* **2010**, *18*, 2325.
[15] M. S. Park, G. X. Wang, Y. M. Kang, D. Wexler, S. X. Dou, H. K. Liu, *Angew. Chem. Int. Ed.* **2007**, *46*, 750.
[16] X. W. Lou, C. M. Li, L. A. Archer, *Adv. Mater.* **2009**, *21*, 2536.
[17] X. Zhou, L. Yu, X. W. Lou, *Adv. Energy Mater.* **2016**, *6*, 1600451.
[18] L. Shen, F. Liu, G. Chen, H. Zhou, Z. Le, H. B. Wu, G. Wang, Y. Lu, *J. Mater. Chem. A* **2016**, *4*, 18706.
[19] H. Wang, X. Lu, L. Li, B. Li, D. Cao, Q. Wu, Z. Li, G. Yang, B. Guo, C. Niu, *Nanoscale* **2016**, *8*, 7595.
[20] Y. Wang, Z. X. Huang, Y. Shi, J. I. Wong, M. Ding, H. Y. Yang, *Sci. Rep.* **2015**, *5*, 9164.
[21] W. S. Kim, Y. Hwa, H. C. Kim, J. H. Choi, H. J. Sohn, S. H. Hong, *Nano Res.* **2014**, *7*, 1128.
[22] R. Z. Hu, Y. P. Ouyang, T. Liang, H. Wang, J. Liu, J. Chen, C. H. Yang, L. C. Yang, M. Zhu, *Adv. Mater.* **2017**, *29*, 1605006.
[23] A. Schoedel, Z. Ji, O. M. Yaghi, *Nat. Energy* **2016**, *1*, 16034.
[24] A. Schoedel, M. Li, D. Li, M. O'Keeffe, O. M. Yaghi, *Chem. Rev.* **2016**, *116*, 12466.
[25] Y. Yang, S. Wang, C. Jiang, Q. Lu, Z. Tang, X. Wang, *Chem. Mater.* **2016**, *28*, 2417.
[26] L. Wang, Y. Han, X. Feng, J. Zhou, P. Qi, B. Wang, *Coord. Chem. Rev.* **2015**, *307*, 361.
[27] G. Zhang, S. Hou, H. Zhang, W. Zeng, F. Yan, C. C. Li, H. Duan, *Adv. Mater.* **2015**, *27*, 2400.
[28] G. Huang, D. Yin, L. Wang, *J. Mater. Chem. A* **2016**, *4*, 15106.
[29] M. S. Yao, W. X. Tang, G. E. Wang, B. Nath, G. Xu, *Adv. Mater.* **2016**, *28*, 5229.
[30] F. Song, K. Schenk, X. Hu, *Energy Environ. Sci.* **2016**, *9*, 473.
[31] Z. Wang, Z. Wang, W. Liu, W. Xiao, X. W. Lou, *Energy Environ. Sci.* **2012**, *6*, 87.
[32] F. Fan, G. Fang, R. Zhang, Y. Xu, J. Zheng, D. Li, *Appl. Surf. Sci.* **2014**, *311*, 484.
[33] Z. Wang, Z. Wang, H. Wu, X. W. Lou, *Sci. Rep.* **2013**, *3*, 1391.
[34] Y. Cao, L. Zhang, D. Tao, D. Huo, K. Su, *Electrochim. Acta* **2014**, *132*, 483.
[35] S. Han, Y. C. Pu, L. Zheng, L. Hu, J. Z. Zhang, X. Fang, *J. Mater. Chem. A* **2015**, *4*, 1078.
[36] K. Zhao, L. Zhang, R. Xia, Y. Dong, W. Xu, C. Niu, L. He, M. Yan, L. Qu, L. Mai, *Small* **2016**, *12*, 588.
[37] A. Aijaz, J. Masa, C. Rösler, W. Xia, P. Weide, A. J. R. Botz, R. A. Fischer, W. Schuhmann, M. Muhler, *Angew. Chem. Int. Ed.* **2016**, *55*, 4087.

[38] N. Lavanya, S. Chinnathambi, *RSC Adv.* **2016**, *6*, 68211.
[39] M. Y. Cho, S. B. Yoon, K. B. Kim, D. S. Jung, K. C. Roh, *RSC Adv.* **2016**, *6*, 37923.
[40] X. Zhu, M. Liu, Y. Liu, R. Chen, Z. Nie, J. Li, S. Yao, *J. Mater. Chem. A* **2016**, *4*, 8974.
[41] F. Zheng, Y. Yang, Q. Chen, *Nat. Commun.* **2014**, *5*, 5261.
[42] S. Vijayakumar, S. H. Lee, K. S. Ryu, *RSC Adv.* **2015**, *5*, 91822.
[43] H. Liu, S. Chen, G. Wang, S. Z. Qiao, *Chem. - Eur. J.* **2013**, *19*, 16897.
[44] H. Liu, D. Su, R. Zhou, B. Sun, G. Wang, S. Z. Qiao, *Adv. Energy Mater.* **2012**, *2*, 970.
[45] Q. Su, J. Zhang, Y. Wu, G. Du, *Nano Energy* **2014**, *9*, 264.
[46] W. S. Kim, Y. Hwa, H. C. Kim, J. H. Choi, H. J. Sohn, S. H. Hong, *Nano Res.* **2014**, *7*, 1128.
[47] L. Xia, S. Wang, G. Liu, L. Ding, D. Li, H. Wang, S. Qiao, *Small* **2016**, *12*, 853.
[48] X. W. Liu, X. W. Zhong, Z. Z. Yang, F. S. Pan, L. Gu, Y. Yu, *Electrochim. Acta* **2015**, *152*, 178.

Received: May 9, 2017
Revised: June 23, 2017
Published online: